AIP CONFERENCE PROCEEDINGS 288

LASER ABLATION: MECHANISMS AND APPLICATIONS–II

SECOND INTERNATIONAL CONFERENCE

KNOXVILLE, TN APRIL 1993

EDITORS:

JOHN C. MILLER

DAVID B. GEOHEGAN

SOLID STATE DIVISION
OAK RIDGE NATIONAL LABORATORY

AIP PRESS

American Institute of Physics New York

L.C. Catalog Card No. 93-73040
ISBN 1-56396-226-8
DOE CONF-9304144

Printed in the United States of America.

ENERGY COUPLING AND DISSIPATION MECHANISMS IN LASER-SOLID INTERACTION

A. Vertes
The George Washington University, Washington, DC 20052

ABSTRACT

A one dimensional hydrodynamic model of laser ablation and plume breakdown is presented. The energy coupling mechanisms include linear light absorption in solid, liquid and vapor phase, thermal and optical runaway, avalanche breakdown and electron-neutral and electron-ion inverse Bremsstrahlung (IB). Results are discussed for KrF and XeCl excimer laser ablation of $YBa_2Cu_3O_{7-x}$ targets in vacuum, XeF excimer laser ablation of copper in vacuum and in background gas. The evolution of plume breakdown and consequent surface screening is demonstrated. Development of hot shock front and expansion slowdown is observed in the presence of background gas. Also, the thermal load on guest molecules in matrix assisted laser desorption is evaluated. The temperature history of the surface shows a short (approximately double pulse length) temperature spike.

INTRODUCTION

Large scale mathematical modeling of laser ablation started in the early seventies with attempts to describe laser fusion in solid hydrogen targets [1]. Major efforts have been devoted during the following years to understand and characterize the interaction of high irradiance laser pulses with a variety of solids. These studies typically covered the $>1GW/cm^2$ laser irradiance region and sought the most efficient way of reaching ever higher plasma temperatures. In this plasma heating regime the portion of deposited energy spent on volatilization is usually a small fraction of energy associated with ionization and plasma heating. Consequently most of the related models neglect the condensed phase processes.

Preparative and analytical laser ablation on the other hand capitalize on non-equilibrium phase transitions induced by the very high heating rate of Q-switched lasers. By the end of the eighties several ablation applications showed promising results and prompted in-depth investigations.

Laser ablation was part of the pulsed laser deposition technique, a promising contender for producing films of strategic materials such as diamond or high-transition temperature superconductors [2,3]. In this method rapid laser heating of the target results in non-equilibrium vapor composition that in turn leads to the deposition of non-stoichiometric layers on the substrate. Vast array of new materials with custom tailored properties can be synthesized this way.

In the processing of structured thin layers, laser treatment also offered unique features. For example in the oxygen atmosphere annealing step of superconducting $YBa_2Cu_3O_{7-x}$ layers the extreme fast heating and cooling rates make it possible to

reach the necessary surface temperature without substantially changing the bulk temperature. This selectivity has its obvious advantages in dealing with complex microstructures.

Another breakthrough related to laser-solid interaction came from the field of analytical chemistry. For decades there was an obstacle for the gas phase investigation of large (bio)molecules. Above a certain molecular weight, it was impossible to volatilize these substances, precluding the application of powerful spectroscopic and separation techniques in their investigation. The introduction of matrix-assisted laser desorption (MALD) provided a unique possibility to induce phase transition. As a result, mass spectrometric (MS) investigation of very large molecules became possible. The MALD-MS method features unprecedented accuracy in the molecular mass determination of proteins up to several hundred thousand Dalton molecular mass [4,5].

The general application of laser sampling of solids for analytical purposes also is in the introductory phase. Preliminary results are available for laser sampling in combination with inductively coupled plasma mass spectrometry [6] and with glow discharge mass spectrometry [7] for the analysis of metals, glasses, ceramics, and other hard-to-analyze insulators. The technique is far from maturity, but indications of its superior analytical sensitivity and versatility are already apparent.

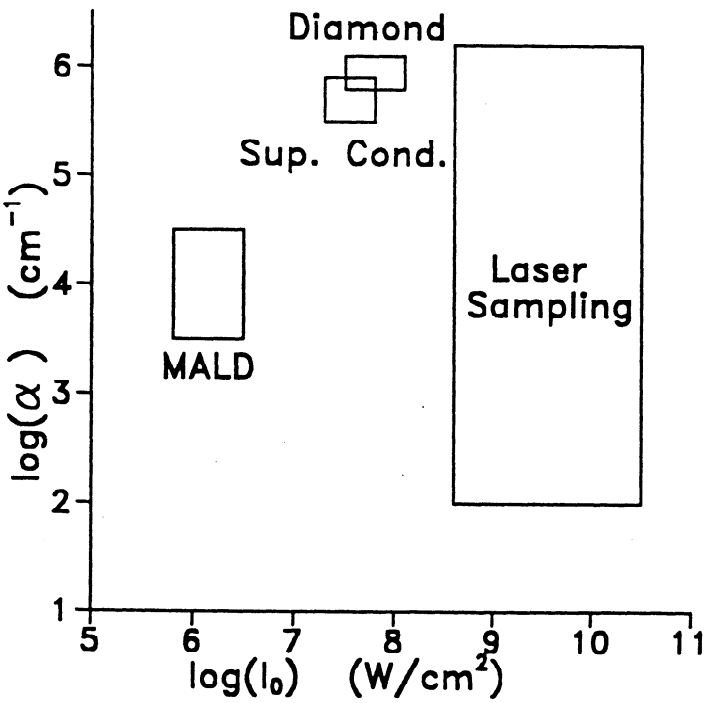

Fig. 1. Map of deposited power density in some important applications of laser induced processes.

The relationship between these applications of laser-solid interaction is apparent if we display the associated laser irradiances, I_0, and light absorption coefficients, α, as it is illustrated in Figure 1. Desorption like mild interactions (MALD: matrix-assisted laser desorption) are clearly separated from ablation processes (Sup. Cond.: pulsed laser deposition of high temperature superconductor layers; Diamond: synthetic diamond formation) and from plasma generation (Laser Sampling of solids for analytical purposes).

HYDRODYNAMIC MODEL

Laser ablation applications rely on lasers working in the moderate irradiance regime (10^6 -10^{10} W/cm^2). Depending on the governing energy deposition and redistribution processes several phases of the interaction can be distinguished. The interaction of Q-switched laser pulses with solids can be treated as three or four stage process. These stages are separated by the onset of various phase transitions and plasma ignition.

Assuming thermal mechanism in *Phase 1* the absorbed laser light elevates the target temperature. This process is governed by the optical and thermal properties of the solid. Optical reflection and absorption coefficients, thermal conductivity and specific heat are the principal parameters characterizing this process. The two energy coupling optical parameters are susceptible to self-induced variations. Thermal and optical "runaway" in semiconductors and avalanche breakdown in insulators can drastically enhance the energy deposition efficiency. In multicomponent or molecular systems thermalization may be hindered due to bottlenecks in the energy transfer scheme.

Energy is dissipated solely through conductive losses in the solid. Radial transport can be neglected as long as the laser beam is moderately focused. The time development of axial temperature distribution, T(x,t), is described by the one-dimensional heat conduction equation accounting only for transfer along the axis perpendicular to the target surface:

$$\frac{\partial T(x,t)}{\partial t} = \frac{\partial}{\partial x}\left[\left(\frac{K_s}{c_p^s \varrho_s}\right)\frac{\partial T(x,t)}{\partial x}\right] + \frac{\alpha_s}{c_p^s \varrho_s} I_0(t)\,(1-R_s)\exp(-\alpha_s x) \quad (1)$$

where α_s, R_s, ρ_s, c_p^s and K_s are optical absorption and reflection coefficients, density heat capacity and thermal conductivity of the solid phase, respectively. $I_0(t)$ denotes the temporal variation of laser irradiance during the pulse.

Phase 2 starts when the surface temperature reaches the melting point or the sublimation temperature. Surface evaporation generates a transient plume above the target while the liquid-solid interface penetrates into the bulk. The heat conduction equation has to be solved separately for the molten phase:

$$\frac{\partial T(x,t)}{\partial t} = \frac{\partial}{\partial x}\left[\left(\frac{K_l}{c_p^l \varrho_l}\right)\frac{\partial T(x,t)}{\partial x}\right] + \frac{\alpha_l}{c_p^l \varrho_l} I_0(t)\,(1-R_l)\exp(-\alpha_l x) \quad (2)$$

where the material parameters of Eq.(1) are reindexed with "l" sub- or superscript indicating the appropriate values for the liquid phase.

If the flux of particles, j, leaving the molten surface can be described by thermally activated surface vaporization the process is governed by the surface temperature, T_s:

$$j(T_s) = \frac{\beta p_0}{\sqrt{2\pi MRT_s}} \exp\left(\frac{\Delta H_{lv}(T_s - T_{lv})}{RT_s T_{lv}}\right) \qquad (3)$$

β denotes the so called sticking coefficient of surface molecules with M molecular mass. ΔH_{lv} and T_{lv} are the enthalpy and temperature of the liquid-vapor phase transition at p_0 ambient pressure.

The plume is optically thin in this phase, its energy stems only from transfer of hot material across the vapor-liquid interface. Gas phase dissipation processes involve expansion cooling and heat conduction. Under certain conditions evaporation recoil pressure may lead to melt ejection. Explosive ejection of material also can be observed due to volume evaporation of the superheated molten layer or as a consequence of thermally induced stress relaxation [8]. *Phase 3* starts when the plume density cannot be neglected and hydrodynamic expansion effects become relevant. The plume expansion is followed by using the conservation of mass, momentum and energy [9,10,11]:

$$\frac{\partial \varrho_v}{\partial t} = -\frac{\partial(\varrho_v v)}{\partial x} \qquad (4)$$

$$\frac{\partial(\varrho_v v)}{\partial t} = -\frac{\partial(p + \varrho_v v^2)}{\partial x} \qquad (5)$$

$$\frac{\partial\left[\varrho_v\left(e + \frac{v^2}{2}\right)\right]}{\partial t} = -\frac{\partial\left[\varrho_v v\left(e + \frac{p}{\varrho_v} + \frac{v^2}{2}\right)\right]}{\partial x} + \alpha_v I_0(t) \exp(-\alpha_v x) - \varepsilon_{rad} \qquad (6)$$

where ϱ, $\varrho_v e$, v, p and α_v denotes the density, internal energy density, hydrodynamic velocity, pressure and light absorption coefficient of the vapor, respectively. The ϵ_{rad} power loss is calculated assuming only Bremsstrahlung radiation. The $\alpha_v = \alpha_{e,n} + \alpha_{e,i}$ absorption coefficient has two components: the electron-neutral, $\alpha_{e,n}$, and the electron-ion, $\alpha_{e,i}$, inverse Bremsstrahlung contributions.

If the irradiance exceeds the plasma ignition threshold additional energy coupling occurs due to breakdown of the plume. In the initial stage of this phase ion densities are low, thus electron-neutral inverse Bremsstrahlung contributes to the plume absorption. As the plume gets more and more ionized electron-ion inverse Bremsstrahlung takes over as the main absorption mechanism. The plume may become fully ionized and consequently optically thick. This is the beginning of an optional *Phase 4* in the interaction, when the vapor phase is completely ionized and totally absorbs the incoming laser light. Ion generation in the model is treated as the consequence of thermoionic emission from the heated surface and as thermal ionization in the vapor. These processes are described by the Langmuir-Saha and

Saha-Eggert equations, respectively. It is at this stage when surface shadowing by the plasma can be observed. Energy is dissipated through radiative loss and expansion in the plume and via heat conduction in the condensed phases.

The different energy deposition processes and the corresponding light absorption coefficients are summarized in Table I.

Table I Energy deposition processes and light absorption coefficients

Process	Light absorption coefficient
Linear absorption of solid	$\alpha_{s,0}$
Thermal runaway (semiconductors)	$\alpha_s=\alpha_{s,0}+n_{eh}(T)\sigma_{eh}$
Optical runaway (semiconductors)	$\alpha_s=\alpha_{s,0}+n_{eh}(I)\sigma_{eh}$
Avalanche breakdown (insulators)	$\alpha_s=\alpha_{s,0}+n_{eh}(T)\sigma_{eh}$
Linear absorption of liquid	$\alpha_{l,0}$
Linear absorption of vapor	$\alpha_{v,0}$
Electron-neutral IB	$\alpha_{e,n}=[1-\exp(h\nu/kT)]\sigma_n n_e n_n$
Electron-ion IB	$\alpha_{e,i}=[1-\exp(h\nu/kT)]\times$ $\times(4e^6/3hc\nu^3m_e)(2\pi/3m_ekT)^{1/2}n_e\Sigma z^2n_zg_z$

$n_{eh}(T)$, $n_{eh}(I)$ and σ_{eh} denote the temperature and irradiance dependent electron-hole number density and electron-hole photon absorption cross section, respectively. σ_n is the cross section of the absorption of a ν frequency photon by an electron during its interaction with neutral species n. n_e, n_n and n_z stand for the number density of electrons, neutrals and the z-th ionic species respectively. g_z is the appropriate Gaunt factor.

We have to emphasize that the four phases of the model cannot be separated in time due to substantial overlap between some of them. Therefore, all equations have to be solved simultaneously and the solutions for the vapor, liquid and solid regions have to satisfy coupling boundary conditions. This is a remarkable departure from many of the previous models, where the individual stages were handled independently [12,13].

RESULTS AND DISCUSSION

KrF and XeCl excimer laser ablation of $YBa_2Cu_3O_{7-x}$ targets show similar ablation thresholds independent of the laser wavelength [14,15]. Surface etching experiments [14] with XeCl laser at 308 nm show the onset of plume formation between 0.20 J/cm^2 and 0.27 J/cm^2. Similarly, KrF ablation [15] of $YBa_2Cu_3O_{7-x}$ at 248 nm starts at around 0.2 J/cm^2.

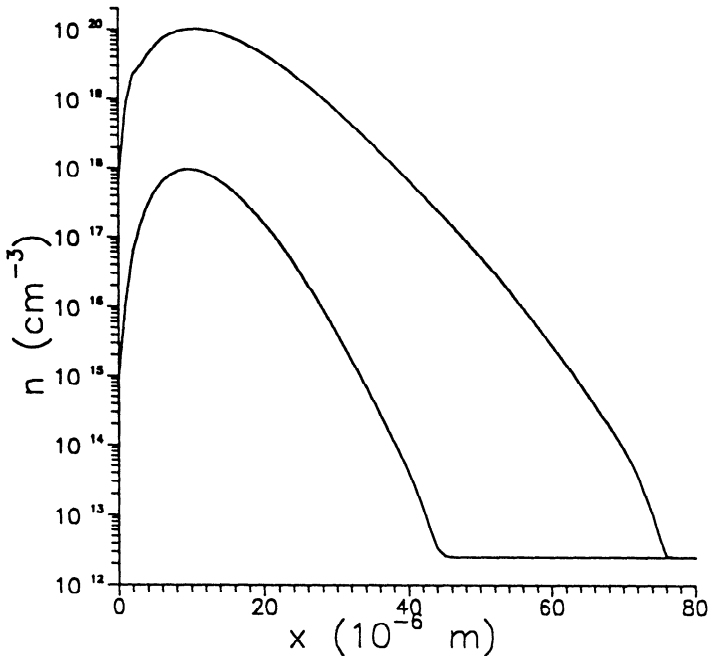

Fig. 2. Plume density distributions at KrF and XeCl laser ablation of $YBa_2Cu_3O_{7-x}$ targets (40 ns frame).

Plume density distributions were calculated using the previously described model at 10 and 20 MW/cm^2 irradiances for 17 ns KrF and XeCl lasers. The density distributions (shown in Fig. 2.) were almost identical for the different lasers but showed dramatic differences between the different irradiances. Based on our calculations substantial plume formation starts somewhere between 0.17 J/cm^2 (lower curve) and 0.34 J/cm^2 (upper curve) fluence for *both lasers*. Twofold increase in laser fluence yields almost two orders of magnitude rise in plume density. This range shows good correlation with the experimental values mentioned above. The lack of laser specificity can be explained taking into account the weak dependence of energy coupling absorption and reflection coefficients ($\alpha=2.3x10^5cm^{-1}$; $R=0.07$)[14] in the 248-308 nm spectral region for $YBa_2Cu_3O_{7-x}$. In the vicinity of the ablation threshold the plume is optically thin therefore the strong wavelength dependence of IB processes can be neglected.

Velocity distributions show variations depending on method of investigation, followed species and applied laser irradiance [16]. Fluorescence transients of neutral Y, Ba, Cu, and O excited states yielded $\sim 10^6$ cm/s velocities, laser ionization mass spectroscopy of Y and BaO at 7×10^9 W/cm^2 indicated $<6\times10^5$ cm/s values, whereas transient optical absorption spectroscopy of Y, Ba, Cu, and Ba^+ at 5×10^7 W/cm^2 showed velocities between 3×10^5 cm/s and 5×10^5 cm/s depending on the species [16]. Inspection of the plume velocity distributions at 2×10^7 W/cm^2 reveals 4×10^4 cm/s center of mass velocity and 2×10^5 cm/s maximum velocity. The lower calculated velocities may be attributed to the considerable difference between laser irradiances. Calculated velocity distributions show substantial increase with increasing irradiance [11].

Excimer laser ablation of copper also has been extensively studied by different plasma diagnostic techniques including laser induced fluorescence (LIF) [17] and Langmuir probe measurements [18]. Extensive evaluation of the effect of ruby laser irradiation on copper target showed encouraging agreement with experimental data[11]. Description of plasma ignition at copper vacuum interface due to XeF laser pulses by our model also has been compared to LIF data and to the extension of a laser fusion model [19] in a separate publication [20]. Here we present data on the early

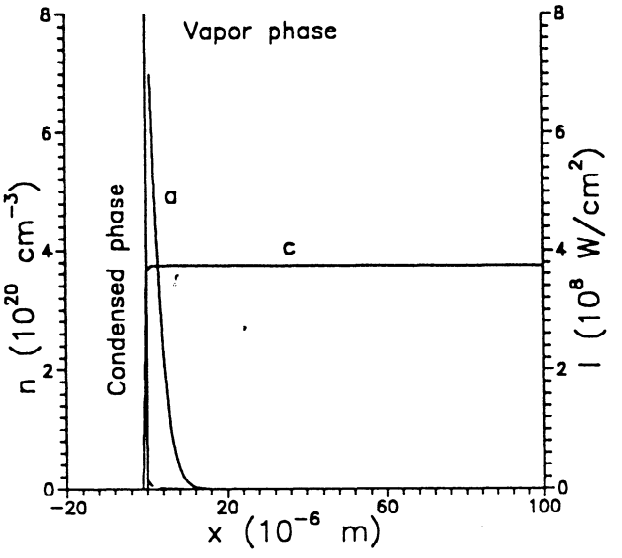

Fig. 3/a. Vapor density (a) and laser irradiance (c) profiles at copper/vacuum interface.

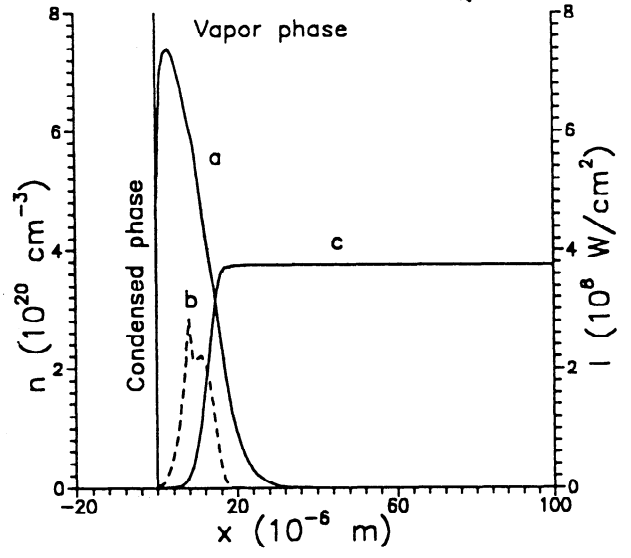

Fig. 3/b. By the 10 ns time stage the total number density of ions and neutrals (a) is comparable to the electron number density (b). The laser irradiance (c) sharply drops in the vapor.

development of vapor breakdown and on the effect of ambient gas pressure on the expansion.

In Figure 3 we demonstrate how light intensity profiles and density distributions change due to plasma formation. Figure 3/a shows the 5 ns time stage of the 375 MW/cm^2 XeF excimer laser pulse. The laser light fully penetrates the plume, its energy is absorbed by the copper surface. The electron number density is low compared to the density of neutrals. They cannot be plotted on the same linear scale. At this stage only electron-neutral IB couples laser energy to the plume. This is a relatively inefficient process causing only moderate heating. It is important to point out, however, that during the early phases of interaction this is the only direct absorption mechanism in the vapor. The related light absorption coefficient (see Table I) is proportional to neutral number densities. Thus, the dense neutral plume is the driving force of electron-neutral IB.

At 10 ns Figure 3/b shows a very different interaction. The electron and ion number density increased substantially due to emission from the solid and to thermal ionization in the plume. As a consequence strong electron-ion IB absorption takes over. Laser irradiance drops sharply inside the plume moving the hot layer about 10 μm in front of the target. This effect, called surface shadowing, has double effect on the target. Due to the lack of laser heating surface temperature and vapor pressure drop. The plume density distribution exhibits a maximum. At more elevated laser irradiances the plume temperature increases dramatically and the plume dissipates energy through

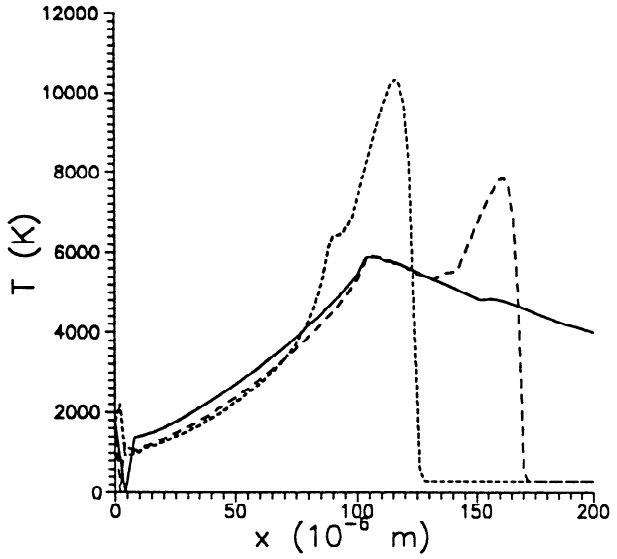

Fig. 4/a. Copper plume temperature distributions in vacuum (solid line) and in background gas (dashed line, dotted line).

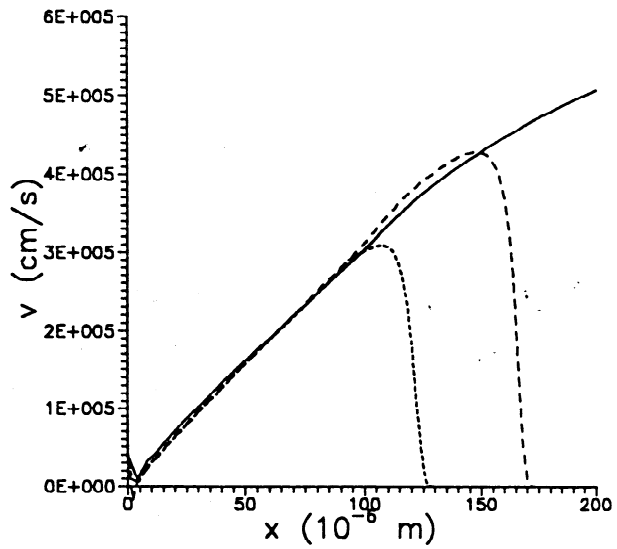

Fig. 4/b. Plume velocity distributions at different background pressures. Slowdown of plume expansion at elevated pressures can be observed.

radiative processes. The energy emitted by the plume can be reabsorbed by the target surface in this self regulating regime.

The presence of background gas during plasma expansion leads to significant changes in plasma structure. Among them are the formation of a luminous shock front at the plasma/background gas interface and the substantial slowdown of the expansion [3]. In order to demonstrate these features in our model we investigated the interaction of a 375 MW/cm^2 XeF excimer laser pulse with copper target at three different background gas particle number densities, n_{bg}. Fig. 4/a shows the copper plume temperature distributions at 40 ns expansion into vacuum ($n_{bg}=10^{13}$cm^{-3}, solid line) and into background gas at different pressures ($n_{bg}=10^{17}$cm^{-3}, dashed line; $n_{bg}=10^{19}$cm^{-3}, dotted line). Formation of a high temperature shock front at the plasma/background gas interface is apparent. (Material and laser parameters are identical with Fig.3. values.) Increasing the background pressure compresses the high temperature region and leads to higher temperatures. Shock front temperatures may substantially exceed plasma temperatures. For example in the $n_{bg}=10^{17}$cm^{-3} case the plasma temperature is ~5800 K whereas the shock front temperature reaches ~7800 K.

Elevated pressures also result in slower expansion as it is apparent from Fig. 4/b. The position of the shock front coincides with the position of velocity drop from maximum value to zero, i.e. with the interface between resting background gas and expanding plasma. As it was pointed out earlier maximum velocities are somewhat lower than some experiments indicate [20].

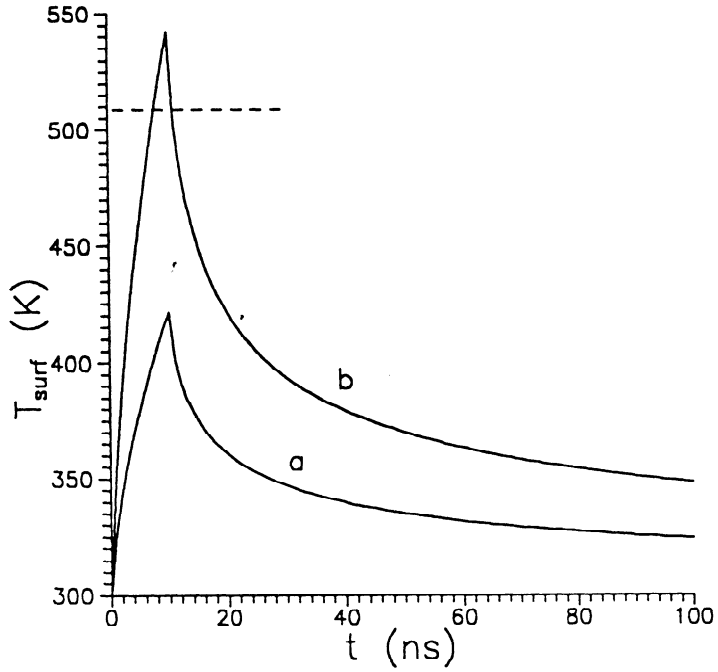

Fig. 5. Surface temperature of nicotinic acid target responding to a 10 ns, 266 nm laser pulse (a, 5 MW/cm^2; b, 10 MW/cm^2).

Matrix assisted laser desorption opened new avenues in the volatilization of large and/or thermolabile molecules. In a continuing effort to understand the underlying mechanism we investigated the thermal load on "probe" molecules embedded in the matrix. A probe molecule experiences two different environments during the desorption process. The first phase is the period while the molecule is still fixed near to the surface of the matrix. As the laser pulse heats the surface the probe molecule is subjected to energy exchange with matrix molecules. As soon as the phase transition releases the probe molecule its environment changes into an expanding and rapidly cooling plume. Plume temperatures can drop to around 100K in 100 ns [21,22]. It is the net effect of the first heating and the second cooling phase that determines the internal temperature of probe molecules. The cooling phase was described earlier. Here we discuss the heating phase.

Fig. 5. shows the surface temperature of nicotinic acid target due to a 10 ns frequency quadrupled Nd-YAG laser pulse (266 nm) at roughly threshold irradiance (a, 5 MW/cm^2) and at higher irradiance (b, 10 MW/cm^2). At threshold irradiance the temperature history of the surface exhibits a short (approximately double pulse length) temperature spike. The surface temperature is below sublimation temperature at all times. Plume formation in this regime is due to elevated vapor pressure above the surface.

The amplitude of the temperature spike is proportional to the laser irradiance. At 10 MW/cm^2 the surface temperature exceeds the phase transition temperature (509 K, indicated by dashed line) for a short time. During this period the surface becomes superheated and explosive phase transition may occur. In this explosive regime the sudden phase transition cuts short the time available for the heating phase.

The relative duration of heating and cooling periods, the corresponding matrix temperatures and energy transfer coefficients determine the thermal load on the embedded and entrained probe molecules. A detailed study of these factors and their influence on MALD is underway.

ACKNOWLEDGEMENT

The author acknowledges helpful discussions with R. W. Dreyfus of IBM Research Division. Support of the National Science Foundation (Grant CTS-9212389) and the George Washington University Facilitating Fund also is greatly appreciated.

REFERENCES

1. P. Mulser, Z. Naturforsch. 25a, 282 (1970).
2. See for example papers in "Laser Ablation for Materials Synthesis", D.C. Paine and J.C. Braviman (eds), Materials Res. Soc. Proc. 191 (1990), Pittsburgh, PA.
3. D.B. Geohegan, Appl. Phys. Lett. 60, 2732 (1992).
4. M. Karas, U. Bahr, F. Hillenkamp, Int. J. Mass Spectrom. Ion Proc., 92, 231 (1989).
5. B. Spengler, R.J. Cotter, Anal. Chem. 62, 793 (1990).
6. E.R. Denoyer, K.J. Fredeen, J.W. Hager, Anal. Chem. 63, 445A (1991).
7. W.W. Harrison, B.L. Bentz, Prog. Analyt. Spectrosc. 11, 53 (1988).
8. A. Vertes, R.D. Levine, Chem. Phys. Letters 171, 284 (1990).
9. A. Vertes, P. Juhasz, M. De Wolf, R. Gijbels, Scanning Microscopy 1988-2, 1853 (1988).
10. A. Vertes, P. Juhasz, M. De Wolf, R. Gijbels, Int. J. Mass Spectrom. Ion Proc. 94, 63 (1989).
11. L. Balazs, R. Gijbels, A. Vertes, Anal. Chem. 63, 314 (1991).
12. D.I. Rosen, D.E. Hastings, G.M. Weyl, J. Appl. Phys. 53, 5882 (1982).
13. D.I. Rosen, J. Mitteldorf, G. Kothandaraman, A.N. Pirri, E.R. Pugh, J. Appl. Phys. 53, 3190 (1982).
14. T. Nakamiya, K. Ebihara, P.K. John, B.Y. Tong, p. 109 in Ref 2.
15. D.B. Geohegan, D.N. Mashburn, R.J. Culbertson, S.J. Pennycook, J.D. Budai, R.E. Valiga, B.C. Sales, D.H. Lowndes, L.A. Boatner, E. Sonder, D. Eres, D.K. Christen, W.H. Christie, J. Mater. Res. 3, 1169 (1988).
16. D.B. Geohegan, Appl. Phys. Lett. 55, 2345 (1989).
17. R.W. Dreyfus, J. Appl. Phys. 69, 1721 (1991).
18. R.J. von Gutfeld, R.W. Dreyfus, Appl. Phys. Lett. 54, 1212 (1989).
19. C.R. Phipps, R.W. Dreyfus in: Laser Ionization Mass Analysis, A. Vertes, R. Gijbels and F. Adams (eds), (Wiley, N. Y., 1993), p. 369.
20. A. Vertes, D. Platt, R.W. Dreyfus, IBM J. of Res. and Dev., submitted.
21. A. Vertes, R. Gijbels in: Laser Ionization Mass Analysis, A. Vertes, R. Gijbels and F. Adams (eds), (Wiley, N. Y., 1993), p. 127.
22. A. Vertes, Gy. Irinyi, R. Gijbels, Anal. Chem., in press.